Catalysis Science & Technology

Selectivity controlled transformation of carbon dioxide into a versatile bi-functional multi-carbon oxygenate using physically mixed ruthenium-iridium catalyst

Journal:	*Catalysis Science & Technology*
Manuscript ID	CY-ART-01-2021-000149.R2
Article Type:	Paper
Date Submitted by the Author:	27-Apr-2021
Complete List of Authors:	Chatterjee, Maya; AIST Tohoku Chatterjee, Abhijit; Dassault Systemes KK BIOVIA Kawanami, Hajime; Interdisciplinary Research Center for Catalytic Chemistry AISTCentral 5
Note: The following files were submitted by the author for peer review, but cannot be converted to PDF. You must view these files (e.g. movies) online.	
Scheme 1.cdx	

Selectivity controlled transformation of carbon dioxide into a versatile bi-functional multi-carbon oxygenate using physically mixed ruthenium-iridium catalyst

Maya Chatterjee[*a], *Abhijit Chatterjee*[c], *Hajime Kawanami*[*b, d]

[a] *Microflow Chemistry Group, Research Institute for Chemical Process Technology, AIST Tohoku, 4-2-1, Nigatake, Miyagino-ku, Sendai, 983-8551, Japan, Tel: 81 22 237 5213; Fax: 81 22 237 5388*

[b] *Interdisciplinary Research Center for Catalytic Chemistry, AIST,Central 5, 1-1-1Higashi Tsukuba, Ibaraki, 305-8565, Japan*

[c] *Dassault Systemes K.K., BIOVIA, Tokyo, Think Park Tower, 2-1-1 Osaki Shinagawa-ku,* 141-6020, *Japan*

[d]*CREST, Japan Science and Technology (JST), 4-1-8, Honcho, Kawaguchi, Saitama,332-0012, Japan*

E-mail: c-maya@aist.go.jp; h-kawanami@aist.go.jp

Abstract

To mitigate environmental concern and energy issues, the conversion of carbon dioxide (CO_2) to valuable and useful carbon chemicals offers a promising strategy for the development of a carbon neutral economy. The utilization of inert CO_2 as a building block in the synthesis of multi-carbon (> 2) oxygenated compounds, specifically propylene glycol methyl ether (PGME; $C_4H_{10}O_2$), produced annually at a multi-million-ton scale from petroleum-based propylene oxide is of particular interest because of its multifaceted industrial and commercial applications. Herein, we present a simple and straightforward system that uses CO_2 in compressed form as the C1 feedstock for the synthesis of PGME by

the direct hydrogenation and subsequent C-C coupling without any other sacrificial reagent. In addition, we combine experimental results with DFT calculations to elucidate synergistic contributions of the two catalytic metals (Ru and Ir) to activate CO_2 for hydrogenation and consequently mediated the C-C bond formation leading to the generation of PGME. Taken together, our findings suggest that the strategy presented herewith may serve as a starting point for the development of a sustainable chemical synthesis platform for multi-carbon oxygenates by utilizing CO_2 as the starting material.

Introduction

The development of an effective method to produce petroleum-derived compounds using a renewable feedstock is emerging as an increasingly important strategy for the synthesis of value-added chemicals. In this context, CO_2 is an attractive renewable C1 feedstock because of its abundance, nontoxicity and nonflammability. However, thermodynamically stable and kinetically inert nature of CO_2 has been a major hurdle to the transformation of this C1 feedstock, which have required high energetic reactants, severe reaction conditions (200 °C or above) and complex designer catalysts.[1-12] If we focus on oxygenated compounds starting from CO_2 produced to date, research efforts have concentrated on the formation of C1 (formic acid, formate, methanol) and C2 (ethanol)[2-12] products. Although, multi-carbon oxygenates (> C_2) are more valuable and display excellent compatibility with gasoline as the blending fraction,[13] the catalytic conversion of CO_2 to multi-carbon oxygenates (> C_2) is still in its infancy due to the involvement of a complex network of hydrogenation and C-C coupling under reducing conditions in a controlled manner[14, 15]. Traditionally, such studies have relied on electro-reduction or high energy reagents (organometallic and strong organic bases) by utilizing additional sacrificial carbon sources, hence produced mixtures of products or have formed by-products, limiting their subsequent applicability.[9-12, 16, 17] As such, there remains a persistent need for the development of straightforward methodologies to selectively synthesize multi-carbon oxygenates (> C2) that are of industrial and commercial interest utilizing CO_2 as starting reactant material.

An example of an industrially relevant and versatile multi-carbon oxygenate is propylene glycol methyl ether (PGME), with a global market value of > $1500 million (USD) in 2017

which is expected to grow further > $2000 million (USD) by 2026. Some of the established uses of PGME include: fuel additives to improve the distillation curve by reducing the emission of particulate matter and NO_x,[18] brake fluids components to improve the responsiveness of brakes, paint, varnish and lacquer components as well as an intermediate for PGME-acetate (which is a photoresist solvent in the semiconductor industry).[19] Traditionally, the industrial production of PGME involves propylene oxide (a petroleum-based highly toxic and hazardous compound) and alcohol, however, as the epoxide ring of propylene oxide may open through either of its C-O bonds, resulting low activity and PGME selectivity.[20] Although, the application of acidic or basic catalysts have improved the selectivity towards PGME, the process still suffers from the several drawbacks including the necessity of liquid waste treatment as well as corrosion problem.[21] As a result, developing an alternative sustainable process that utilizes CO_2 as the starting material is particularly prudent at this time.

Turning CO_2 into a feedstock, requires large amounts of concentrated CO_2 with high purity. Nevertheless, direct recovery of the gas from the atmosphere (e.g., atmosphere; 0.03 vol. %) or exhaust gases from transportation is unfavourable, has high energy penalties, and possesses economical constraints or sometimes is infeasible because of the very low concentrations. Alternative opportunities exist to capture CO_2 in a concentrated form, for example from the exhaust gas of thermal power plants, oil refineries, and industrial chemical plants before it enters the atmosphere.[22] Supercritical CO_2 ($scCO_2$) is more reliable in terms of its availability in pure and concentrated forms, with tuneable hybrid properties of either gaseous or liquid states, which allows the formation of products with higher yields under

comparatively milder conditions, thus, catalytic deactivation and destruction of the reactor system can be prevented. Nonetheless, even after the exemplary work of Jessop *et al.*,[23] $scCO_2$ was rarely explored as a reactant.[24, 25]

Herein, we have designed an approach to produce PGME (multi-carbon oxygenate) utilizing $scCO_2$ as a reactant. To develop a strategy for utilizing $scCO_2$ as a reactant, a laboratory scale verification and validation of predicted performance is critical for securing access to the CO_2 economy. To this end, we utilized $scCO_2$ and hydrogen as the reactants, ruthenium (Ru) and iridium (Ir) as the catalysts because both of the metals (Ru and Ir) were highly efficient towards hydrogenation and C-C coupling reaction. [23, 26, 27] Furthermore, mesoporous silica (MCM-41), which possesses large surface area to increase the effectiveness of the active atoms (surface area is proportional to utilization efficiency) was used as a support material for Ru and Ir. Having developed this system, we began by optimizing the catalyst and the reaction conditions. Finally, we integrated our experimental findings with theoretical calculations to validate the reaction path. Altogether, we were able to successfully synthesize PGME with high-selectivity using a simple and efficient strategy.

Results and discussion

Characterization of catalysts

MCM-41 supported Ru and Ir catalysts were prepared by hydrothermal method and then both of the catalysts were mixed by different mixing processes such as mechanical, chemical and physical (details are in the experimental section). Structural characterization of individual Ru/MCM-41 and Ir/MCM-41 using XRD confirmed the retention of mesoporous structure

even after the incorporation of metals (Supporting information; Fig. S1). Furthermore, mesoporous structure was also preserved in the catalysts obtained from various mixing processes (mechanical, chemical and physical) (Supporting information; Fig. S2a-c). Focusing, on the physically mixed Ru/MCM-41 and Ir/MCM-41 (Ru-Ir-PM) catalysts, existence of mesoporous moiety as well as Ru and Ir were also evident even from the XRD pattern of spent catalysts (Supporting information; Fig. S2d; Fig. S2 inset). In addition, N_2 adsorption-desorption also reflect the typical mesoporosity of the studied Ru-Ir-PM catalysts (Supporting information section).

Morphological analysis of individual Ru/MCM-41 and Ir/MCM-41 is presented in Fig. S3 (Supporting information). The high-angle annular dark-field scanning transmission electron microscopy (HAADF-STEM) image shows two distinct contrasts. The highly contrast part representing the presence of heavy particles inside the silica channels (existence of smaller particles) and the larger bright spots in the darker background of amorphous silica matrix (larger particles). The average particle size of 5.1 and 4.8 nm was determined for Ru/MCM-41 and Ir/MCM-41, respectively. The representative HAADF-STEM images of mechanically and chemically mixed catalysts are also shown in Fig. S4 and Fig. S5 (Supporting information), respectively. For mechanically mixed catalysts, an irregular distribution of metal particles with a mean diameter of 9.5 nm were observed (Supporting information; Fig. S4a). Elemental mapping and the corresponding EDS analysis (Supporting information; Fig. S4b-f) revealed an isolated existence of both metals in a single location. In contrast, the chemically mixed catalyst displayed a uniform distribution of the bimetallic nanoparticles of average size 9.8 nm and featured Ru and Ir adjacent to each other in a selected region (Fig.

S5a-f). Furthermore, Fig. 1 presents montage of HAADF-STEM images, electron mapping and corresponding EDS of Ru-Ir-PM. A representative HAADF-STEM image of fresh catalyst shows dispersion of Ru and Ir throughout the surface depending on locations. Both of the metals largely preserved their crystallinity (Fig. 1a inset) and maintained their individuality even after mixing, which can be best illustrated by EDS of the tested region (Fig. 1b). The spent catalyst also maintained the dispersion and individuality of both metals (Fig. 1c); however, an overlapping signal originates in the selected location designated as region **2** (Fig. 1d and 1e), directed towards the possibility of single particle formation. A high resolution HAADF-STEM images of region **2** (Fig. 1f-1g) labelled with square (green) (Fig. 1g) shows the coexistence of both Ru and Ir, which was again confirmed from the EDS profile (Fig. 1h). The formation of single particle might be due to the segregation of Ru and Ir occurred during the reaction. No alloy particles were detected in any of the cases.

Catalytic performance of single-metal Ru/MCM-41 and Ir/MCM-41 catalysts

Our initial experimental approach was to assess the viability of the single-metal Ru/MCM-41 and Ir/MCM-41 catalysts individually, to design a process for synthesizing multi-carbon oxygenated compound using $scCO_2$ as a reactant with selectivity control. We found that both of the individual catalysts successfully converted $scCO_2$ into methanol, ethanol, 2-propanol and PGME (Fig. 2a and 2b). All of the products were confirmed from the analysis of the condensable liquid phase after reaching the steady state (definition in the experimental section). The product selectivity on Ru/MCM-41[ethanol (65.5%) > PGME (22.0 %) > methanol (11.0 %) > 2-propanol (1.5 %)] varied considerably from Ir/MCM-41 [2-propanol

(92.9 %) > PGME (5.9%) > methanol (0.8%) > ethanol (0.4%)] under the optimized set of screened conditions (total pressure=16 MPa, P_{H2}/P_{CO2}=0.33, reaction time= 16 h), (Fig. 2a). To better understand the catalytic efficiency, the performance of each catalyst was evaluated in terms of molar productivity (mmol g_{cat}^{-1} h^{-1}) and turnover frequency (*TOF; h^{-1}).* On Ru catalyst the efficiency order was: ethanol (0.7 mmol g_{cat}^{-1} h^{-1}; *79* h^{-1}) > PGME (0.3 mmol g_{cat}^{-1} h^{-1}; *34* h^{-1}) > methanol (0.2 mmol g_{cat}^{-1} h^{-1}; *22* h^{-1}) > 2-propanol (0.02 mmol g_{cat}^{-1} h^{-1}; *2* h^{-1}), whereas, on Ir catalyst the efficiency order was: 2-propanol (1.16 mmol g_{cat}^{-1} h^{-1}; *130* h^{-1}) > PGME (0.14 mmol g_{cat}^{-1} h^{-1}; *15h^{-1}*) > ethanol (0.12 mmol g_{cat}^{-1} h^{-1}; *13* h^{-1}) (Fig. 2b). All these results reflected the astounding ability of both the catalysts to generate multi-carbon oxygenated products through hydrogenation and C-C coupling. Analyses of the resultant gaseous products confirmed the formation of methane on both of the single-metal catalysts (Ru= 0.001 mol %; Ir= 0.004 mol %) but CO was below the detection limit (< 6 ppm).

Mixture of Ru/MCM-41 and Ir/MCM-41 catalysts

The implementation of the individual single-metal Ru/MCM-41 or Ir/MCM-41 catalysts resulted in a mixture of compounds rather than a single targeted product, thus, we applied a physical mixture of the Ru/MCM-41 and Ir/MCM-41(Ru-Ir-PM) as catalyst for the conversion of $scCO_2$. It is important to note that a physical mixture of solid catalysts can have significant impact on the product distribution compared to their individual counterparts due to the additive effect (i.e., synergy between the two metals).[28, 29] Fig. 3a shows the catalytic performance of Ru-Ir-PM as a function of composition. Starting from a ratio of 10 % Ru/MCM-41: 90 % Ir/MCM-41 (weight basis), PGME was formed with the selectivity of

30.3 %, and reached a maximum of >99 % at the catalytic composition of 80 % Ru/MCM-41: 20 % Ir/MCM-41. The formation of PGME as a single product was confirmed by GCMS (Supporting information; Fig. S6a-b), ^{1}H (Supporting information; Fig. S7) and ^{13}C NMR (Supporting information; Fig. S8) analysis. In addition, the catalytic efficiency (molar productivity and *TOF*) towards PGME formation, was also maximized at a catalyst composition of 80 % Ru/MCM-41: 20 % Ir/MCM-41, with a value of 3.1 mmol g_{cat}^{-1}h-1(*348* h^{-1}) as compared to 0.2 mmol g_{cat}^{-1} h^{-1} (*22* h^{-1}) and 0.14 mmol g_{cat}^{-1} h^{-1} (*15*h^{-1}) for 100% Ru/MCM-41 and 100 % Ir/MCM-41, respectively (Fig. 3b). These results emphasized (i) the beneficial synergistic effects between the two metals and (ii) the necessity of controlling the catalytic composition efficiently to obtain PGME as the single product.

Different process of mixing: For solid catalysts, the mixing process can greatly influence the catalytic outcome due to possible change in the concentration of metal components or arrangements of the active constituents (ensemble effects).[30] As such, after optimizing the ratio of the individual metal components, we also tested the catalysts prepared *via* mechanical (ball-milling) and chemical (bi-metallic) mixing (Fig. 4). Under the optimized reaction conditions (80 % Ru/MCM-41: 20 % Ir/MCM-41; total pressure=16 MPa, P_{H2}/P_{CO2}=0.33), the mechanically mixed catalyst produced methanol, ethanol and PGME with the selectivity of 34.4%, 14.4% and 51.2%, respectively (Fig. 4). The catalytic efficiency (molar productivity and *TOF*) to produce PGME (0.05 mmol g_{cat}^{-1} h^{-1}; *5.6* h^{-1}) was strikingly low compared to Ru-Ir-PM (3.1 mmol g_{cat}^{-1} h^{-1}; *348* h^{-1}). It is likely that the implementation of mechanical forces modulated the electronic and geometric structure of metal catalyst. In comparison, the chemically mixed catalyst produced 2-propanol and PGME with the

selectivity of 17.6% and 82.4%, respectively. Although, the PGME selectivity (82.4%) was relatively high, the productivity was low (1.2 mmol g_{cat}^{-1} h^{-1}; *135h^{-1}*) compared to Ru-Ir-PM (3.1 mmol g_{cat}^{-1} h^{-1}; *348 h^{-1}*). Taken together, these results suggested that the mixing process had significant impact on the catalytic activity. Despite the same compositions, morphological differences (distribution pattern of Ru and Ir) arise due to the variation of the mixing processes (as mentioned in catalyst characterization section) and have substantial influence on particle size, shape, interaction with support, adsorption-desorption behavior of reactant and products,[31] which might govern the catalytic efficiency and selectivity of the reactions.

Optimization of reaction conditions

Based on the maximum catalytic efficiency, we continued our studies with the Ru-Ir-PM catalyst of the composition that maximized PGME selectivity (i.e., 80 % Ru/MCM-41: 20 % Ir/MCM-41) for optimization of different reaction parameters (e.g., total pressure, P_{H2}/P_{CO2} ratio and reaction time) related to catalytic performances. As our target was to develop a system under mild reaction conditions so we have chosen the temperature of 150 °C for parametric optimization required to obtain measurable catalytic activity for the studied reaction.

Variation of total reactant pressure: First, the effect of total reactant pressure on the product distribution was investigated at a fixed temperature of 150 °C (Fig. 5a). PGME remained the predominant product throughout the entire pressure range studied (8 MPa- 20 MPa). The selectivity of PGME was changed from 88.1% (8 MPa) to >99 % (16 MPa), which

then decreased to 73.7 % at 20 MPa due to unexpected formation of ethanol. Alteration of pressure invoked a strong influence on PGME productivity that increased from 0.46 mmol g_{cat}^{-1} h^{-1}; *52.0h^{-1}* (8 MPa) to 3.1 mmol g_{cat}^{-1} h^{-1}; *348 h^{-1}* (16 MPa) and then dropped to 0.37 mmol g_{cat}^{-1} h^{-1}; *41.6h^{-1}* (20 MPa) (Fig. 5a). This pressure-based performance, emphasized the density inhomogeneity of $scCO_2$ (P= 8 MPa, *d*=2.332 mol/l; P= 16 MPa, *d*=5.0772 mol/l; calculated using Peng-Robinson EOS) that is, with decreasing pressure, CO_2 preferred to exist in a low dense gas-like state, but with increasing pressure, CO_2 preferred to exist in a densified liquid-like state as verified by video monitoring performed under the conditions relevant to all reactions (Supporting information; Fig. S9a-e). The fluctuation of PGME selectivity and productivity above 16 MPa was attributed to the liquid-like state, which enabled the desorption of intermediate other than required for PGME formation. Intriguingly, the highest PGME productivity was achieved at a total reactant pressure of 16 MPa corresponding to the liquid-like density of CO_2, which causes a possible change in the adsorption-desorption behavior of reactants and products crucial for heterogeneous catalysis (Fig. 5b).

Variation of P_{H2}/P_{CO2} ratio: Having selected a total pressure of 16 MPa as the optimized total pressure for PGME formation at a fixed temperature of 150 °C, we next investigated the effect of P_{H2}/P_{CO2} ratio on the catalytic performances, varies from 0.041 to 0.6. Fig. 6a shows PGME as the only detectable product throughout the entire range studied. However, we noticed a significant role of P_{H2}/P_{CO2} ratio on PGME productivity, which switched from 0.26 mmol g_{cat}^{-1} h^{-1}; *29.2h^{-1}* (P_{H2}/P_{CO2}= 0.041) to 0.03 mmol g_{cat}^{-1} h^{-1}; *3.4h^{-1}* (P_{H2}/P_{CO2}= 0.6) after attaining maximum of 3.1 mmol g_{cat}^{-1} h^{-1}; *348 h^{-1}* (P_{H2}/P_{CO2}= 0.33). This significant lowering

of the PGME productivity at higher P_{H2}/P_{CO2} ratio could be attributed to the hydrogenation of surface C1 species prior to coupling. Fig. 6b compares the PGME productivity and methane concentration (via gaseous product analysis) as a function of P_{H2}/P_{CO2} ratio. At the higher P_{H2}/P_{CO2} ratio of 0.6, the simultaneous reduction of PGME productivity (3.1 mmol g_{cat}^{-1} h^{-1} to 0.03 mmol g_{cat}^{-1} h^{-1}) and enhanced methane concentration (0.002 mol% to ~ 4 mol %), (Supporting information; Fig. S10a and S10b) reflected the preference for hydrogenation of C1 species due to the higher availability of hydrogen.[32] In particular, although, a more detailed account of the effect of P_{H2}/P_{CO2} ratio on the reaction could be obtained by constructing a solubility model (as reported previously for the hydrogenation reaction using CO_2 as co-solvent [33, 34]), such a model cannot be extrapolated to the high temperatures used in this reaction system. Regardless, control over the P_{H2}/P_{CO2} ratio was critical to increase the productivity of PGME formation.

Time profiles of mixed catalysts: After the confirmation of reactant pressure and P_{H2}/P_{CO2} ratio, we evaluated the time profile for the Ru-Ir-PM catalyst (Fig. 7). Within 1h, the resultant product mixture contained methanol, ethanol and 2-propanol with the selectivity of 4.2%, 43.3% and 52.5%, respectively. In 2h, methanol disappeared completely, the selectivity of ethanol and 2-propnol were also reduced to 33.6% and 39.9%, respectively, whereas, PGME was detected with a selectivity of 26.5%. Over the next 4h, PGME became the only detectable product that reached the highest selectivity of > 99 % and then remained constant. Initially (after 1h), the catalytic efficiency followed the order of: 2-propanol (0.7 mmol$g_{cat}^{-1}h^{-1}$; *78.6h*$^{-1}$) > ethanol (0.27 mmol g_{cat}^{-1} h^{-1}; *30.0h*$^{-1}$) > methanol (0.13 mmol g_{cat}^{-1} h^{-1}; *15.0h*$^{-1}$) suggesting the preference for C-C coupling over hydrogenation on Ru-Ir-PM. Furthermore,

as the time increased from 2h to 16h, a substantial enhancement of PGME productivity (*TOF*) from 0.09 mmol g_{cat}^{-1} h^{-1} (*10.0h^{-1}*) to 3.1 mmol g_{cat}^{-1} h^{-1} (*348 h^{-1}*) was attained. The robustness of the catalyst was evidenced from its efficiency after 72h of reaction with a trivial change of PGME productivity from 3.1 mmol g_{cat}^{-1} h^{-1} to 2.8 mmol g_{cat}^{-1} h^{-1} (Fig. 7) due to the slight increase in methane concentration as observed from the analysis of gaseous product (Supporting information; Fig. S11). Due to the differences in catalytic performance based on the mixing process, we proceeded to study the time-profile of the reaction on both mechanically and chemically mixed catalysts. Our kinetic investigations demonstrated two different product distribution trends related to the mechanical (Supplementary Fig. S12a) and chemical mixing processes (Supplementary Fig. S12b). For mechanically mixed catalysts, in 1h, methanol and ethanol were formed with the selectivity of 72.5% and 27.5%, respectively (Fig. S11a). PGME was detected with a selectivity of 18.2% after 2h, which then reached to 51.2% with prolonging the reaction time of 16h along with methanol (34.4%) and ethanol (14.4%). No propanol was detected throughout the studies. Although, the molar productivity and *TOF* of PGME formation increased from 4 x 10^{-3} mmol g_{cat}^{-1} h^{-1} (*0.44h^{-1}*) to 0.05 mmol g_{cat}^{-1} h^{-1} (*5.6h^{-1}*), the results suggested a relatively slow rate of product formation after mechanical mixing of the Ru and Ir catalysts. On the other hand, chemically mixed catalyst (Supporting information Fig. S11b) showed no detectable products during 1h of reaction. After 2h, ethanol, 2-propanol and PGME were evident with the selectivity of 22.9%, 36.2% and 40.9%, respectively. Upon extending the reaction time to 16h, ethanol was disappeared and the selectivity of 2-propanol was also dropped to 17.6% but PGME reached a maximum selectivity of 82.4%. Moreover, the molar productivity and *TOF* of PGME were also

increased from 0.07 mmol g_{cat}^{-1} h^{-1} (*8.0h^{-1}*) to 1.2 mmol g_{cat}^{-1} h^{-1} (*135 h^{-1}*) as the reaction time was changed from 2h to 16h. Thus, compared to the catalytic efficiency of the mechanically mixed catalyst towards PGME formation (4 x10^{-3}mmol g_{cat}^{-1} *0.46* h^{-1}; *h^{-1}*), a significant enhancement was evident on chemically mixed catalysts (1.2 mmol g_{cat}^{-1} h^{-1}; *135 h^{-1}*).

Different product distribution on the catalysts from various mixing processes are indicative of different reaction pathways (hydrogenation and C-C coupling) occurring at different rates. Despite the same metal content, differences in the mixing process result significant changes in the catalytic performance and determines the product distribution. Catalytic structure and its relation with activity is a critical as well as a challenging issue, which rely on the concentration of metal components or arrangements of the active constituents (ensemble effects) related to electronic and geometric structure of key elements. Thus, understanding of such correlation need separate attention. Based on the highest productivity of PGME, Ru-Ir-PM was considered as a superior catalyst than its mechanical and chemical analogs with the same composition under the studied reaction conditions. Notably, there was no reaction right after the addition of reactants in any of the cases.

Proposed reaction path of PGME formation

The time profile of Ru-Ir-PM (Fig. 7) evidences the (i) formation of methanol, ethanol and 2-propanol within 1h as initial products and also highlights (ii) the gradual disappearance of those initial products with the formation of PGME. For the first case, simultaneous detection of methanol, ethanol and 2-propanol indicated that the reaction proceeded *via* parallel routes

rather than in a sequential path (methanol→ ethanol →2-propanol), which also confirmed from the control experiments (Supporting information; Table S1; Entry 1-2). From the second case, we expected the possible involvement of methanol, ethanol and 2-propanol on the PGME formation. Thus, control experiments were performed with defined amount (10 mmol) of methanol, ethanol and 2-propanol as probe compounds along with $scCO_2$ and hydrogen (Supplementary Table S1; Entry 1-3). Result shows that $scCO_2$ was successfully converted into PGME with > 99% selectivity in the presence of methanol, which remain inactive (Supplementary Table S1; Entry 1). Considering ethanol as a probe compound, diethoxyethane was the major product of selectivity 79.4% along with PGME (20.6%) (Supplementary Table S1; Entry 2). On the other hand, incorporation of 2-propanol, results no PGME and isopropyl acetate was the sole product (selectivity > 99%) (Supplementary Table S1; Entry 3). Notably, diethoxyethane and 2-propyl acetate were reported to form by the reaction between CH_3CHO with ethanol[35] and 2-propanol[36], respectively. Additional experiments with CH_3CHO, which produced ethanol (59.3%), 2-propanol (21.3%), ethyl acetate (10.0%) and diethoxyethane (9.4%) (Supplementary information; Table 1; Entry 6), confirmed its intermediacy.[37] Hence, results of control experiments suggested the existence of CH_3CHO in the system. However, we did not observe this compound during our $scCO_2$ hydrogenation experiments possibly due to the instrumental limitations and high reactivity of CH_3CHO.

We collated our experimental findings to derive a reaction pathway for the transformation of $scCO_2$ to PGME on Ru-Ir-PM (Scheme1). PGME was formed from $scCO_2$ and hydrogen through the hydrogenation and C-C coupling reaction. Catalytic hydrogenation of CO_2

generally proceeds *via* formate or CO pathway. We hypothesized the formate pathway for CO_2 hydrogenation under the present condition as CO was below the detection level during the studies. The hypothesis was further validated through the two separate reactions using HCHO (possible intermediate of formate pathway) and CO (0.2 MPa) as substrates. Under the same conditions applied for $scCO_2$ hydrogenation, HCHO was transformed into methanol (Supplementary information; Table S1; Entry 4), whereas, no products were detected from CO (Supplementary information; Table S1; Entry 5). Altogether these results were consistent with the notion that the hydrogenation of $scCO_2$ proceeded *via* the formate pathway [38] on Ru-Ir-PM. Detection of methanol was notable only on Ru (0.14 mmol g_{cat}^{-1} h^{-1}) (Fig.1), hence, preference for hydrogenation of HCHO on Ru surface can be suggested, that corresponds well with the previous reports.[39] The extent of HCHO hydrogenation strongly depend on the reduction of RuO_2 to Ru^0, [40] The existence of RuO_2/Ru^0 (RuO_2 =85 % and Ru^0 =15 %) in Ru-Ir-PM was confirmed from the XPS analysis (details are in the Supporting information section; Fig. S13a-d), as low loading of Ru has a tendency for partial reduction [41], hence, hydrogenation of HCHO to methanol was restricted. Therefore, considering the experimental findings, it is reasonable to suggest that instead of further hydrogenation, the HCHO species generated from the hydrogenation of $scCO_2$ on catalyst surface,[42] coupled to form structure **I** preferably on Ir site of Ru-Ir-PM. The propensity for C-C coupling on Ir site was reported earlier [43, 44]. In addition, the rapidity of 2-propanol (C3) formation on Ir/MCM-41 (1.16 mmol g_{cat}^{-1} h^{-1}; *130* h^{-1}) compared to Ru/MCM-41 (0.02 mmol g_{cat}^{-1} h^{-1}; *2* h^{-1}Fig. 2b) also displayed inclination for C-C coupling on Ir site. Thus, in Ru-Ir-PM, Ir, which is existed as IrO_2 (confirmed from the XPS studies; details are in the Supporting information section)

motivating the coupling reaction [45] to form structure **I**, which was then transformed into structure **II** after the shifts of hydrogen and consequent rearrangement [46] that explain the generation of CH_3CHO intermediate (Scheme 1). Furthermore, the results from our control experiments were also revealed that CH_3CHO is an active intermediate generated from CO_2 and hydrogen [47, 48] on Ru-Ir-PM. In the following steps, the chain propagation was proposed to involve the nucleophilic attack of an adsorbed formyl on structure **II** yielding C_{n+1} species (structure **III)**, which then transformed into an enolate (structure **IV**) after the shifts of hydrogen atoms and subsequent hydrogenation [49] on Ir surface. Negative enolate ion was then stabilized on positively charged catalytic surface species (RuO_2), and consequently transformed into PGME by the attack of methoxy species *via* anti-Markovnikov fashion to the less substituted carbon.[50] Alternatively, depending on the Ir content in Ru-Ir-PM, the enolate may take up H^+ and further hydrogenated to 2-propanol (Fig. 3).

DFT calculations

To gain further insight into the role of each of the catalytic components (Ru, Ir) and to validate our experimental findings, we performed density functional theory (DFT) calculations. To develop a comprehensive model, the optimized adsorption geometries of the concerned molecules on the individual catalysts with different oxidation states were computed (Supporting information; Fig. S14). In addition, activation energies of concerned reaction paths and the corresponding transition states are also calculated and presented in Table S2 and Fig. S15, respectively (Supporting information). Furthermore, Fig. 8a compares the reaction energy profiles of different steps involved in PGME formation on RuO_2 and IrO_2 surfaces. It is important to note that the reaction energies of each path vary

from one metal to another. For instance, after adsorption, CO_2 was hydrogenated to produce CH_2O species. The calculated reaction energy and activation energy (E_a) (Supporting information; Table S2) for this reaction were -1.30 eV (E_a= 0.39 eV) and -1.18 eV (E_a= 0.59 eV) on RuO_2 and IrO_2, respectively, which confirmed that the RuO_2 surface was energetically preferable for CH_2O formation. The generated CH_2O species, rather than being hydrogenated to methanol on RuO_2 surface (E_a=0.49 eV), can undergo C-C coupling to form a CH_3CHO intermediate on IrO_2 surface with the reaction energy of -2.05 eV (E_a=0.33 eV). This CH_3CHO intermediate can be further hydrogenated to ethanol on RuO_2 [51] with the reaction energy of -2.83 eV (E_a= 0.46 eV) that explained the high *TOF* of ethanol on Ru/MCM-41 (*79* h^{-1}) rather than on Ir (*13* h^{-1}) [IrO_2 = -1.71 eV (E_a= 0.82 eV)] also in agreement with the previous report.[52] Prior to the generation of CH_3CHO, structure **II** underwent chain propagation through a formyl attack and formed structure **III**, where formyl species was generated on IrO_2 surface with the reaction energy of -2.13 eV. Subsequently, structure **III** formed a negatively charged enolate species (structure **IV**). In the final step, stabilization of the enolate ion on the positively charged RuO_2 followed by PGME formation was corroborated by the lower reaction energy on RuO_2 [-2.19 eV; E_a= 0.39 eV] compared to IrO_2 [-1.03 eV; E_a= 0.79 eV]. We also calculated the reaction energy on Ru^0 and Ir^0 for the same reaction paths of PGME formation from CO_2 (Figure 8b); logical for the system containing hydrogen. The hydrogenation of CO_2 to CH_2O species is exothermic with the reaction energies of -0.57 eV (E_a=0.46 eV) and -1.22 eV (E_a=0.52 eV) on Ru^0 and Ir^0, respectively. Further coupling of CH_2O species leads to the formation of CH_3CHO on Ir^0 corresponded to the reaction energy of -2.05 eV (E_a=0.38 eV), whereas, on Ru^0 was -1.89 eV

(E_a=0.51 eV) (Fig. 8b). It has been observed that almost each step is need to bypass high energetic hurdle compared to their oxide counterpart (Supporting information; Table S2). Interestingly, enolate as a non-stabilized species[53] had a high propensity to take up H^+ to form 2-propanol was energetically preferred on Ir^0 (Ir^0=-2.34 eV; E_a=0.44 eV), which explained the rapidity of 2-propanol formation on the Ir/MCM-41 ($130h^{-1}$) compared to Ru/MCM-41 ($2h^{-1}$) as well as on Ru-Ir-PM depending on Ir content (Fig. 2b). Although, it is too early to predict precisely the active sites for the involved reaction steps in the conversion of CO_2 to PGME, combined approach (theoretical and experimental) highlighted the importance of oxidic species rather than the reduced metal. Overall, based on the energetics, the DFT analyses confirmed that the formation and stabilization of reaction intermediates involved in the conversion of CO_2 to PGME that requires synergy of both the metals, which provide the multiple active sites for hydrogenation and coupling reactions to promote the activation of the reactants and the ability of chain propagation to achieve PGME formation with excellent selectivity and productivity.

Conclusion

Here, we have shown that utilization of $scCO_2$ as a prospective reactant for the synthesis of organic compounds can be drastically improved and likely goes beyond the conventional hydrogenation of CO_2 to form C1 and C2 compounds. Our findings revealed PGME as a single product, which was obtained from the combination of $scCO_2$, hydrogen and highly robust catalysts based on physically mixed Ru/MCM-41 and Ir/MCM-41 at a comparatively low temperature of 150 °C required for the conversion of CO_2 to multi-carbon compound.

The process seems particularly promising without the requirement of any additional reagents or solvents, which have typically flattened the environmental benefits of CO_2 as a feedstock. This method facilitated the energetically constrained reaction sequence required to produce a multi-carbon oxygenate and also avoids hydrocarbon generation. By combining our experimental results with DFT calculations, we propose a plausible mechanism of the conversion of CO_2 to PGME. This alternative strategy of PGME formation may open up many opportunities to utilize CO_2 to mitigate the energy and environmental issues involved in the traditional synthesis of multi-carbon compounds. This platform may enable further exploration of multi-carbon syntheses with CO_2 as feedstock upon additional investigation of similar catalytic systems and mechanistic pathways. Altogether, this work posits a novel method to utilize $scCO_2$ as a feedstock for fuels and chemicals considering environmental perspectives by adopting new strategies and efficient catalysts to make desired product.

Acknowledgements H. K. is funded by the Japan-U.S. cooperation project for research and standardization of Clean Energy Technologies, The Ministry of Economy Trade and Industry (METI), CREST and Japan Science and Technology (JST).

Materials and methods

Materials: Tetraethyl orthosilicate, sodium hydroxide and ruthenium (III) chloride n-hydrate were purchased from Wako Pure Chemicals. Cetyltrimethylammonium bromide and dihydrogen hexachloroiridate (IV) hydrate were purchased from Merck and Alfa-Aesar, respectively. CO_2 (>99.99%) and hydrogen has been provided by the Nippon Sanso Co. Ltd.

Catalyst preparation: The Ru and Ir catalyst supported on mesoporous MCM-41 was synthesized by the *in-situ* method of metal introduction.[54] This protocol involves tetraethyl orthosilicate (TEOS) and cetyltrimethylammonium bromide (CTAB) as a silica source and a templating agent, respectively. Incorporation of metals were conducted with the aqueous solution of corresponding metal salts such as ruthenium (III) chloride n-hydrate and dihydrogen hexachloroiridate (IV) hydrate. Hydrothermal synthesis of Ru and Ir containing MCM-41 was accomplished from the gel mixture of molar composition: SiO_2: xRu/Ir salt: 0.14 CTAB: $0.56Na_2O$: $120H_2O$, where x is the desired amount of metal to be introduced. The gel was prepared through the addition of 1.30g of CTAB in 52g of deionized water containing 0.54g of NaOH under stirring at ambient temperature for 1h to obtain a clear solution. To this solution, 5g of TEOS was added and then stirring was continued for another 1h. After that required amount of metal salt solution was added slowly to the surfactant and silica mixture with continuous stirring until homogeneity was achieved (2h). The pH of the gel was maintained at 11.3 using sodium hydroxide (NaOH). The resultant gel was autoclaved for 48h at 140 °C. After that autoclave was quenched with water at room temperature. The resulting solid was separated by filtration and washed thoroughly with deionized water followed by drying at 50 °C for overnight. Prior to use, template (CTAB)

was removed from the synthesized material after calcining in air at 550 °C for 8h. Physically mixed catalyst was prepared by blending of calcined Ru/MCM-41 and Ir/MCM-41 of desired ratio (wt. basis) at room temperature by hand without adding any external forces. For ball-milled catalyst, milling was performed in a planetary ball mill at a rotation speed of 150 rpm for 2 h using 10 mm diameter stainless balls at a ball-to-sample weight ratio of 10:1. On the other hand, bimetallic Ru-Ir catalysts was synthesized by the same approach adopted for monometallic catalysts. Instead of a single metal salt solution, a mixture with the desired ratio of both metal precursor solution was added following the same sequence as described for individual metals. Catalysts were obtained in ten different batches with the reproducibility of ± 5%. In each case, metal content was controlled to ~1 wt. % based on gel composition and then confirmed from the elemental analysis.

Catalyst Characterization techniques

Different spectroscopic techniques were employed for structural characterization of developed catalysts. X-ray diffraction (XRD) measurements were conducted with Rigaku Smart lab X-ray diffractometer (Cu-Kα source, 40 kV, 30 mA). In general, the diffraction data were collected using continuous scan mode with a scan speed of 2 deg./min over the scan range of 2θ = 1.5-15° and 2θ = 20-90° for low and wide-angle, respectively. For textural analysis, N_2-adsorption measurements were carried out using a micromeritics ASAP 2400 analyser. The volume of adsorbed N_2 was normalized to standard temperature and pressure. Before experiment, samples were degassed at 300 °C for one night. The specific surface area was determined from the linear part of the BET plot (P/P_0 = 0.05–0.30).

One of the most important technique to visualize the mixture of supported metal nanoparticles is the scanning transmission microscopy (STEM) in combination with bright field (BF) and high-angle annular dark field (HAADF-STEM) technique. Images acquired with Z-contrast and high-resolution standout very clear on a light background of Si and oxygen. As Z contrast imaging is used in HAADF-STEM, the change in contrast depending on the atomic number of the element (Ru=44 and Ir=77) created notable difference of the images to determine the distribution of each element. TEM images, HAADF-STEM, STEM-EDS were conducted using TITAN^{3TM} G2 60-300 (FEI) operated at 300 kV equipped with STEM-mode with Super-X detector. Energy dispersive spectroscopy (EDS) analysis was performed with the ESPRIT imaging software (Bruker).

XPS spectra were recorded on an Ulvac PHI 5601ci spectrometer. The pressure in the sample chamber was kept under 1 x 10^{-7} MPa. The binding energy scales were adjusted to the highest C (1*s*) peak position equal to 284.9 eV. Monochromatized Al *K*α X-ray (14 kV, 200 W) was used in place of a conventional X-ray source to obtain high-quality spectra to avoid overlapping of the satellite peaks; thus, uncertainty in the determinations of the peak position and peak area was nullified. An electron flood gun was used as a neutralizer, and the number of acquisitions was maintained at 12 for each analysis. To ensure the accuracy of the data, the XPS system was calibrated using the peaks of Cu ($2P_{3/2}$) and Cu (3*P*) whose binding energies are 932.67 and 75.14 eV, respectively. All of the powder mineral samples were fixed onto a copper sample holder using double-sided sticky tape.

Catalytic performance: The reaction was performed in a 50 ml stainless steel batch reactor placed over a magnetic stirrer in an oven fitted with a fan heater to maintain the constant temperature of 150 °C (Supplementary Fig. S15a-c). Typically, 0.1g of solid catalyst (Ru-Ir-PM) was incorporated inside the reactor, which contains a stirrer bar for continuous stirring the content during the reaction. After the stabilization of required temperature (generally takes 90 min.), the reactor was pressurized by 4 MPa of hydrogen and then completed the required total pressure of 16 MPa with CO_2. A back-pressure regulator used to maintain the reaction pressure inside the reactor and a pressure monitor for monitoring pressure inside the reactor. Meanwhile, we prepared a collecting vessel in a cold trap (ice-acetone mixture; -5.5 °C) to collect condensable products, which was attached to the outlet of backpressure regulator. Depending on the required reaction time, the reactor was allowed to attain room temperature and the gasses from the reactor started to pass to the collecting vessel slowly through the backpressure regulator until the pressure had the same value in both places (reactor and collecting vessel) (steady state). In each case, products were detected from the analysis of condensable liquid products after reaching the steady state using headspace-GCMS. For gaseous products, samples were collected after attaining the steady state using a Tedlar sampling gas bag and then analysed by GC-TCD (Shimadzu GC-8A equipped with one molecular sieve column and one Porapak Q column). The solid catalyst was then ready for recycling. Each experimental result are average values from three measurements with a reproducibility of ± 10 %. Carbon balance was calculated using the formula of moles of carbon in products (gaseous + condensation) /moles of carbon in reactant. Carbon balance for this reaction was floated from 93 % to 98%. In order to avoid contamination and cross-

correlation between experimental reactants and products, we performed a blank test before each experimental trial. In addition, we performed a blank run prior to product analysis to ensure identities of the products formed. In this way, we were able to avoid contamination in the reaction products.

GCMS analysis for liquid products: The analyses were carried out with Agilent 6890/5973 *inert* MSD (Mass Selective Detector) system. Headspace was performed with an Agilent G1888MS auto-sampler equipped with a 1-ml sample loop. GC (HP 6890) was equipped with VF-WAXms column (J&W, 60 m x 0.25 mm, 0.50 μm) and a flame ionization detector. The GC method used was as follows: an initial oven temperature of 40 °C was held for 2 minutes. In the next step, the temperature was ramped at 10 °C/min. until it reached 230 °C and held for 5 minutes. An ion source temperature of 230 °C, and a column flow rate of 0.70 mL/min using helium at 10 psi as a carrier gas. Before sampling the sample was pre-heated at 50 °C for 20 min. The selectivity to each product was calculated by the following expression $S_i = C_i / \sum Cp$, where C_i is the concentration of the product 'i' as monitored by GC and $\sum Cp$ is the total concentration of the product (mole). Quantification of the products was obtained by a multi-point calibration curve for each product. Productivity and turnover frequency were calculated as follows:

Productivity of PGME= amount of PGME (mmol)/g of catalyst used/h

Turnover frequency *(TOF)*= amount of product produced/ total amount of metal used x time.

NMR analysis: Solution-state spectra of resultant liquid product were acquired using a Bruker 400 MHz AVANCE III spectrometer. ^{1}H NMR (400 MHz, D_2O): δ 5.52 (s, -OH), 4.1-4.3 (m, -OCH_3CH_2CH), 1.94, 1.93 (d, -CH_3). ^{13}C NMR (100 MHz, D_2O): δ 71.35, 65.92, 58.32, 18.33.

Phase observation: The phase behavior of scCO_2 and hydrogen at 150 °C was studied separately in a 10 ml high pressure view cell (Supplementary Fig. S16 d). After the stabilization of temperature, hydrogen at a fixed pressure was introduced into the cell followed by the introduction of CO_2 to reach the desired pressure. For phase observation during the reaction, the content was stirred continuously. All images were recorded during stirring to observe the change in the state of reactants.

Calculation of density: Gas densities were calculated by a chemical engineering process simulator COCO (AmsterCHEM version 3.2) using Peng-Robinson equation of state. Graboski and Daubert have modified the coefficients in the SRK EOS and provided a special relation for hydrogen. This modification of the Soave-Redlich-Kwong equation of state (SRK EOS) has been recommended by the American Petroleum Institute (API). The uncertainty was estimated as 0.5% from the difference between experiment and calculation.

Computational methodology: The calculations were performed on a (100) surface model with 4 layers thickness created from bulk structure of RuO_2 and IrO_2. The initial geometry of the adsorbed molecules was calculated over (100) RuO_2, IrO_2 and their hydrogenated (Ru^0, Ir^0) surfaces using Adsorption Locator Module (Dassault Systemes BIOVIA) that allows finding out the low energy adsorption sites on both periodic and non-periodic substrates as well as investigations on the preferential adsorption of mixtures of adsorbate components.

The Adsorption Locator module identifies possible adsorption sites by carrying out Monte Carlo searches of the configurational space of the substrate-adsorbate system as the temperature is slowly decreased within the simulated annealing process of a molecular dynamics run. [55, 56] The minimum energy structures obtained from the Monte Carlo method were then fully optimized with DFT method as described below.

All the reaction energy calculations were performed using density functional theory (DFT) [57] using DMol^3 [58, 59] of DASSAULT SYSTEMES BIOVIA. Gradient corrected functional BLYP [60, 61] and DNP basis set [62] with spin unrestricted option was used throughout the calculation. The initial spin states were decided according to the spin states of the metal cations present model. The Kohn–Sham equation was expanded in a double numeric[57] quality basis set with polarization functions (DNP). The orbital cutoff range and Fermi smearing were selected as 5.0 Å and 0.001 Ha, respectively. The self-consistent-field (SCF) procedures were performed to obtain well-converged geometrical and electronic structures at a convergence criterion of 10-6 a. u. The energy, maximum force, and maximum displacement convergence were set to 10-6 Ha, 0.002 Ha/Å, and 0.005 Å, respectively. The activation energy was calculated using the transition state search algorithm as implemented in DMol^3 with nudged elastic band method (NEB).

References

1. Z. Li, J. Wang, Y. Qu, H. Liu, C. Tang, S. Miao, Z. Feng, H. An and C. Li, *ACS Catal.* 2017, **7**, 8544−8548.
2. G. H. Gunasekar, K. Park, K.-D. Jung and S. Yoon, *Inorg. Chem. Front.,* 2016, **3**, 882–895.
3. G. Centi, E. A. Quadrelli and S. Perathoner, *Energy Environ. Sci.* 2013, **6**, 1711–1731.
4. M. D. Porosoff, B. Yan and J. G. Chen, *Energy Environ. Sci.* 2016, **9**, 62–73.
5. A. Álvarez, A. Bansode, A. Urakawa, A. V. Bavykina, T. A. Wezendonk, M. Makkee, J. Gascon and F. Kapteijn, *Chem. Rev.* 2017, **117**, 9804−9838.
6. S. Li, Y. Xu, Y. Chen, W. Li, L. Lin, M. Li, Y. Deng, X. Wang, B. Ge, C. Yang, S. Yao, J. Xie, Y. Li, X. Liu and D. Ma, *Angew. Chem. Int. Ed.,* 2017, **56**, 10761 – 10765.
7. S. Kuld, M., Thorhauge, H. Falsig, C. F. Elkjaer, S. Helveg, I. Chorkendorff and J. Sehested, *Science,* 2016, **352**, 969-973.
8. M. Aresta, A. Dibenedetto and E. Quaranta, *J. Catal.,* 2016, **343**, 2-45.
9. A. Banerjee, G. R. Dick, T. Yoshino and M. W. Kanan, *Nature,* 2016, **531**, 215-220.
10. L. Yu, J. Huang and Y. Wang, *ChemCatChem*, 2018, **10**, 4853-4867.
11. J. Wu, S. Ma, J. Sun, J. I. Gold, C. S. Tiwary, B. Kim, L. Zhu, N. Chopra, I. N. Odeh, R. Vajtai, A. Z. Yu, R. Luo, J. Lou, G. Ding, P. J. A. Kenis and P. M. Ajayan, *Nature Commun.,* 2016, **7**, 13869.
12. E. L. Clark, C. Hahn, T. F. Jaramillo and A. T. Bell, *J. Am. Chem. Soc.,* 2017, **139**, 15848−15857.

13. E. Christensen, J. Yanowitz, M. Ratcliff and R. L. McCormick, *Energy Fuels,* 2017, **25**, 4723–4733.

14. Y. Gao, S. Shizhen, Z. Zhao, H. Tao and Z. Sun, *Acta Phys. -Chim. Sin.,* 2018, **34**, 858–872.

15. A. Banerjee and M. W. Kanan, *ACS Cent. Sci.,* 2018, **4**, 606–613.

16. Q. Qian, M. Cui, Z. He, C. Wu, Q. Zhu, Z. Zhang, J. Ma, G. Yang, J. Zhang and B. Han, *Chem. Sci.*, 2015, **6**, 5685–5689.

17. M. Cui, Q. Qian, Z. He, Z. Zhang, J. Ma, T. Wu, G. Yanga and B. Han, *Chem. Sci.*, 2016, **7**, 5200–5205.

18. B. L. Smith, L. S. Ott, and T. J. Bruno, *Environ. Sci. Technol.,* 2008, **42***,* 7682–7689.

19. Y. D. Chaniago, G. R. Harvianto, A. Bahadori and M. Lee, *Process Saf. Environ. Prot.,* 2016, **103**, 413– 423.

20. H. A. Pecorini and J. T. Banchero, *Ind. Eng. Chem.,* 1956, **48**, 1287–1297.

21. C. De, Q. Cai, X. Wang, J. Zhao and B. Lu, *J. Chem. Technol. Biotechnol.,* 2011, **86**, 105–108.

22. P. G. Jessop and R. Noyori, in Green Chemistry using liquid and supercritical carbon dioxide, edited by J. M. DeSimone and W. Tumas; Oxford press, **2003**; Ch. 3 pp. 48-61.

23. P. G. Jessop, T. Ikariya and R. Noyori, *Nature*, 1994, **368**, 231-233.

24. S. Wesselbaum, U. Hintermair and W. Leitner, *Angew Chem. Intl. Edn.,* 2012, **51**, 8585-8588.

25. Z. He, Q. Qian, Z. Zhang, Q. Meng, H. Zhou, Z. Jiang and B. Han, *Phil. Trans. R. Soc. A,* 2015, **373**, 20150006.

26. W. Reeve and A. Sadle, *J. Am. Chem. Soc.*, 1950, **72**, 1251-1254.

27. M. Inoue, T. Miyake, T. Inui and Y. Takegami, *J. Chem. Soc. Chem. Commun.*, 1983, 70-72.

28. G. C. Bond, *Platinum Metals Rev.*, 1983, **21**, 16-18.

29. Y. Wang, S.-L. Chen, Y.-L. Gao, Y.-Q. Cao, Q. Zhang, W.-K. Chang and J. B. Benziger, *ACS Catal.* 2017, **7**, 5572-5584.

30. J. Wang, G. Li, Z. Li, C. Tang, Z. Feng, H. An, H. Liu, T. Liu and C. Li, *Sci. Adv.,* 2017, **3**, e1701290.

31. L. Liu and A. Corma, *Chem. Rev.,* 2018*,* **118***,*4981–5079.

32. K. P. Kuhl, E. R. Cave, D. N. Abram and T. F. Jaramillo, *Energy Environ. Sci.,* 2012, **5**, 7050–7059.

33. E. Bogel-Łukasik, R. Bogel-Łukasik, K. Kriaa, I. Fonseca, Y.Tarasenko, M. Nunes da Ponte, A. Paiva and G. Brunner, *Green Chem.*, 2007, **9**, 427–430.

34. E. Bogel-Łukasik, R. Bogel-Łukasik, K. Kriaa, I. Fonseca, Y.Tarasenko and M. Nunes da Ponte, *J. Supercrit. Fluids*, 2008, **45**, 225–230.

35. M. R. Capeletti, L. Balzano, G. de la Puente, M. Laborde and U. Sedran *Appl. Catal. A General,* 2000, **198**, L1-L4.

36. T. Kunugi and T. Kono, *J. Soc. Chem. Ind. Japan*, 1969, **72**, 1282-1289.

37. F. Hayashi, M. Tanaka, D. Lin and M. Iwamoto, *J. Catal.,* 2014, **316**, 112-120.

38. M. Hus, D. Kopac, N. S. Stefancic, D. L. Jurkovic, V. D. B. C. Dasireddy and B. Likozar, *Catal. Sci. Technol.*, 2017, **7**, 5900–5913.

39. M. Karamad, H. A. Hansen, J. Rossmeisl and J. K. Nørskov, *ACS Catal.,* 2015, **57**, 4075-4081.

40. S. Wang, E. T. Schrunk, H. Mahajan and R. J. Farrauto, *Catalysts,* 2017, **7**, 88-101.

41. S. Coman, M. Florea, F. Cocu, V. I. Parvulescu, P. A. Jacobs, C. Danumah and S. Kaliaguine, *Chem. Commun.*, 1999, 2175-2176.

42. S. Kattel, P. Liu and J. G. Chen, *J. Am. Chem. Soc.,* 2017, **139**, 9739– 9754.

43. M.-Y. Ngai, A. Barchuk and M. J. Krische, *J. Am. Chem. Soc.,* 2007, **129**, 280-281 and references therein.

44. K. Koda, T. Matsu-ura, Y. Obora, and Y. Ishii, Chem. Lett., 2009, **38**, 838-839 and references therein.

45. L. Yang, J. Huang, J. Cen, D.-L. Chen, H. Zeng, Z. Rui, R. Luque and P. Duane, *J. Mater. Chem. A,* 2021, **9**, 7094-7101.

46. A. Kiennemann, H. Idriss, R. Kieffer, P. Chaumette and D. Durand, *Ind. Chem. Res.,* 1991, **30**, 1130-1138.

47. R. Kortlever, J. Shen, K. Jan, P. Schouten, F. Calle-Vallejo and M. T. M. Koper, *J. Phys. Chem. Lett.,* 2015, **6**, 4073−4082.

48. M. E. Fakley and R. A. Head, *Appl. Catal.* 1983, **5**, 3-18.

49. T. J. Mazanec, *J. Catal.*, 1986, **98**, 115-125.

50. W. Zhang, H. Wang, Q. Li Q. Dong, N. Zhao, W. Wei and Y. Sun *Appl. Catal. A: General,* 2005, **294**, 188-196.

51. J. Jae, W. Zheng, A. M. Karim, W. Guo, R. F. Lobo and D. G. Vlachos, *ChemCatChem*, 2014, **6**, 848 – 856.

52. S. Li, Y. Xu, Y. Chen, W. Li, L. Lin, M. Li, Y. Deng, X. Wang, B. Ge, C. Yang, S. Yao, J. Xie, Y. Li, X. Liu and D. Ma, *Angew. Chem. Int. Ed.,* 2017, **56**,10761 –10765.

53. T. Graening and J. F. Hartwig, *J. Am. Chem. Soc.* 2005, **127**, 17192-17193 and references therein.

54. M. Chatterjee, T. Iwasaki, Y. Onodera, T. Nagase, *Catal. Lett.* 1999, **61**, 199-202.

55. N. Metropolis, A. W. Rosenbluth, M. N. Rosenbluth, A. H. Teller and E. Teller, *J. Chem. Phys.*, 1953, **21**, 1087-1092.

56. S. Kirkpatrick, C. D. Gelatt and M. P. Vecchi, *Science*, 1983, **220**, 671-680.

57. W. Kohn and L. Sham, J. *Phys. Rev. A,* 1965, **140**, 1133-1137.

58. B. Delley, *J. Chem. Phys.,* 1990, **92**, 508–517.

59. B. Delley, *J. Chem. Phys.,* 2000, **113**, 7756–7764.

60. A. Becke, *J. Chem. Phys.,* 1988, **88**, 2547-2553.

61. C. Lee, W. Yang and R. G. Parr, *Phys. Rev. B,* 1988, **37**, 785-789.

62. B. Delley, *Phys. Rev. B,* 2002, **66**, 155125-155134.

Legend to figures

Fig. 1: HAADF-STEM images, electron mapping and the corresponding EDS spectra of Ru-Ir-PM. **Before reaction:** (a) HAADF-STEM images and elemental mapping of Ru-Ir-PM of two selected regions and (b) the corresponding EDS. **After reaction:** (c) HAADF-STEM images and elemental mapping; (d) identification of single particle; (e) EDS of selected region; (f-g) High resolution HAADF-STEM images and elemental mapping of single particle; (h) EDS analysis. Elemental mapping of Ru (red), Ir (turquoise) and Si (green).

Fig. 2: Catalytic performance of individual Ru/MCM-41 and Ir/MCM-41catalyst for conversion of CO_2. (a) selectivity and (b) productivity of each products formed. Reaction conditions: Catalysts=0.1g, temperature=150 °C, reaction time=16h and total pressure=16 MPa (P_{H2}= 4 MPa and the rest is CO_2). Each experimental result are average values from three measurements with a reproducibility of ± 10 %

Fig. 3: Comparison of (a) product distribution and (b) productivity of each product on Ru-Ir-PM as a function of mixing ratio. Reaction conditions: Ru-Ir-PM=0.1g, temperature=150 °C, reaction time=16h and total pressure=16 MPa (P_{H2}= 4 MPa and the rest is CO_2). Each experimental result are average values from three measurements with a reproducibility of ± 10 %

Fig. 4: Effect of mixing process on product selectivity and PGME productivity. Physical (Ru-Ir-PM), chemical (bimetallic) and mechanical (ball-milling). Reaction conditions: Catalysts=0.1g, temperature=150 °C, reaction time=16h and total pressure=16 MPa (P_{H2}= 4

MPa and the rest is CO_2). Each experimental result are average values from three measurements with a reproducibility of ± 10 %.

Fig. 5: Evaluation of total pressure on (a) product distribution; (b) PGME productivity; Corresponding reactant phases of reactant are also shown on the right of the graph. Reaction conditions: Ru-Ir-PM=0.1g, temperature=150 °C, reaction time=16h. Each experimental result are average values from three measurements with a reproducibility of ± 10 %

Fig. 6: Plot of P_{H2}/P_{CO2} ratio dependent (a) PGME productivity, selectivity and (b) change of PGME productivity with CH_4 formation. Reaction conditions: Ru-Ir-PM=0.1g, temperature=150 °C, total pressure=16 MPa and reaction time= 16h. Each experimental result are average values from three measurements with a reproducibility of ± 10 %.

Fig. 7: Time dependent product distribution and PGME productivity using Ru-Ir-PM. Reaction conditions: Catalysts=0.1g, temperature=150 °C, total pressure=16 MPa and P_{H2}/P_{CO2}= 0.33. Each experimental result are average values from three measurements with a reproducibility of ± 10 %.

Fig. 8: Calculated energy profiles of each reaction steps are given relative to (a) RuO_2, IrO_2 and (b) Ru^0, Ir^0 of Ru-Ir-PM catalysts to simulate the reaction of CO_2+H_2→ PGME. Each surface is represented by RuO_2 = white; IrO_2 = black; Ru^0= pattern and Ir^0= gray.

Scheme 1: Possible reaction path of PGME formation from CO_2 and H_2 based on experimental results obtained under the present reaction conditions and validated by calculating energies of each step using DFT.

Fig. 1

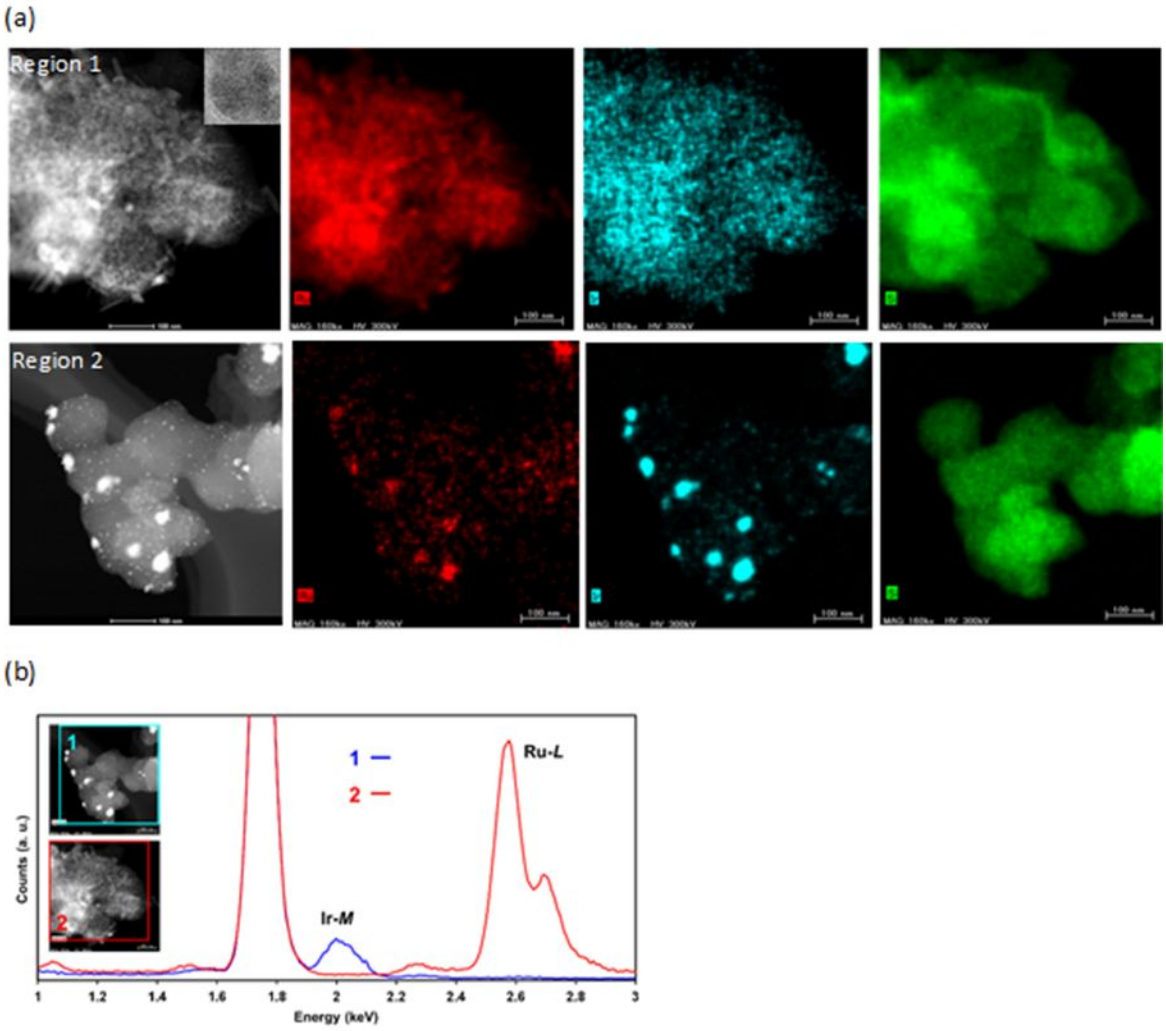
(a)
Region 1
Region 2
(b)
1
2
Ru-L
Ir-M
Counts (a. u.)
Energy (keV)
1
1.2
1.4
1.6
1.8
2
2.2
2.4
2.6
2.8
3

(c)

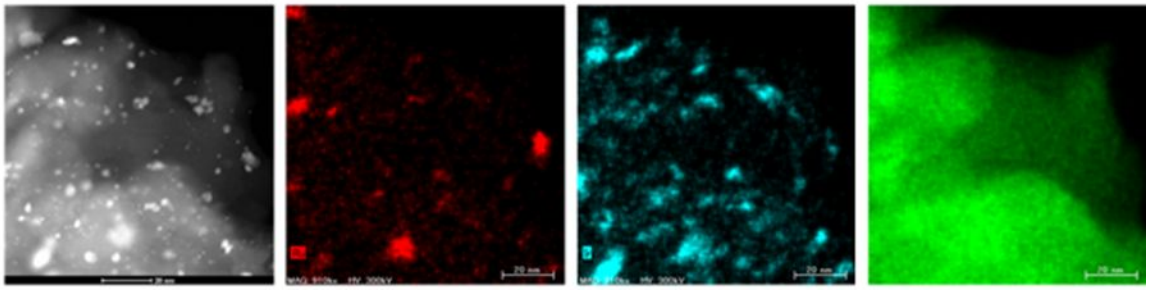

(d)

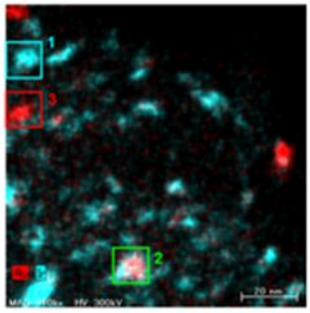
1
3
2

(e)

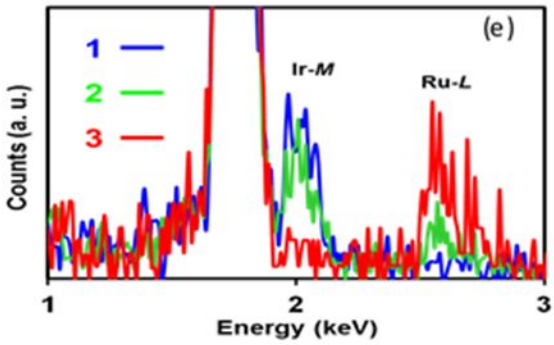
1
2
3
Ir-M
Ru-L
Counts (a. u.)
1
2
3
Energy (keV)

(f)

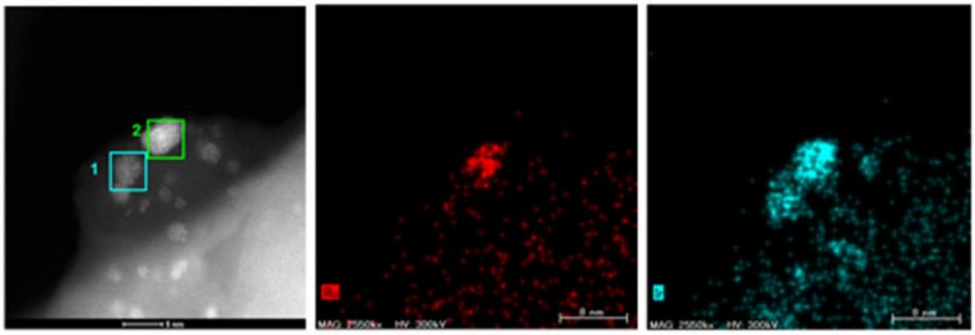
2
1

(g)

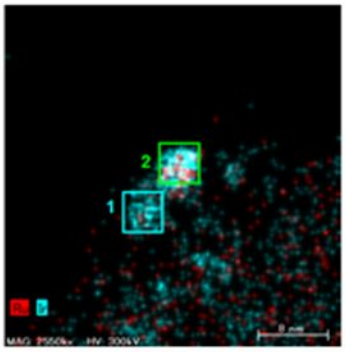
2
1

(h)

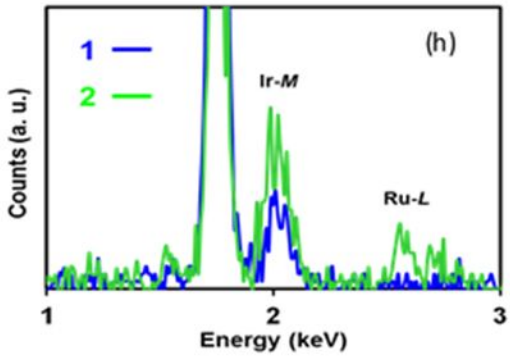
1
2
Ir-M
Ru-L
Counts (a. u.)
1
2
3
Energy (keV)

Fig. 2

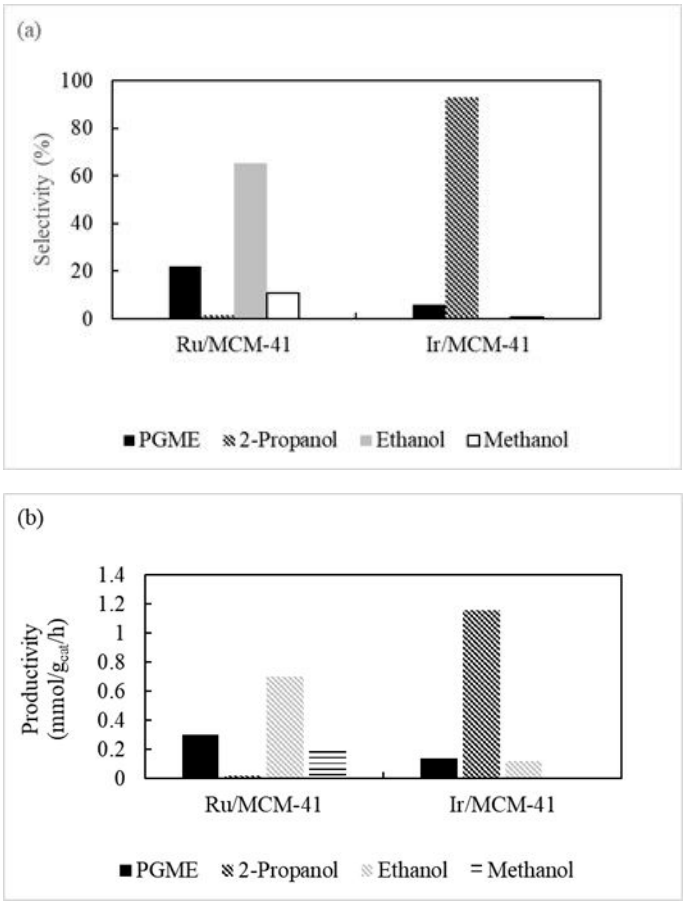
(a)
Selectivity (%)
100
80
60
40
20
0
Ru/MCM-41
Ir/MCM-41
PGME
2-Propanol
Ethanol
Methanol
(b)
Productivity (mmol/g$_{cat}$/h)
1.4
1.2
1
0.8
0.6
0.4
0.2
0
Ru/MCM-41
Ir/MCM-41
PGME
2-Propanol
Ethanol
Methanol

Fig. 3

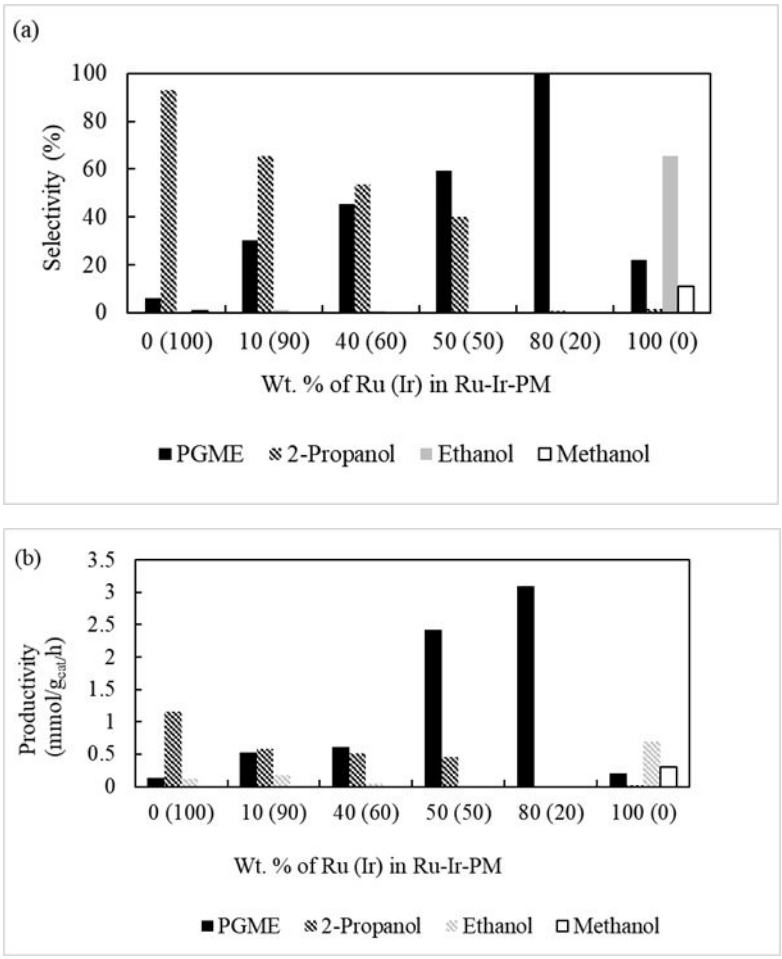
(a)
Selectivity (%)
100
80
60
40
20
0
0 (100)
10 (90)
40 (60)
50 (50)
80 (20)
100 (0)
Wt. % of Ru (Ir) in Ru-Ir-PM
PGME
2-Propanol
Ethanol
Methanol
(b)
Productivity (mmol/g$_{cat}$/h)
3.5
3
2.5
2
1.5
1
0.5
0
0 (100)
10 (90)
40 (60)
50 (50)
80 (20)
100 (0)
Wt. % of Ru (Ir) in Ru-Ir-PM
PGME
2-Propanol
Ethanol
Methanol

Fig. 4

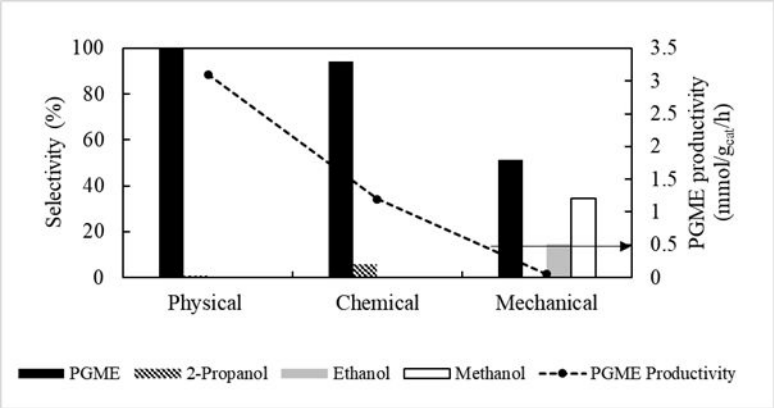
Selectivity (%)
PGME productivity (mmol/g$_{cat}$/h)
100
80
60
40
20
0
3.5
3
2.5
2
1.5
1
0.5
0
Physical
Chemical
Mechanical
PGME
2-Propanol
Ethanol
Methanol
PGME Productivity

Fig. 5

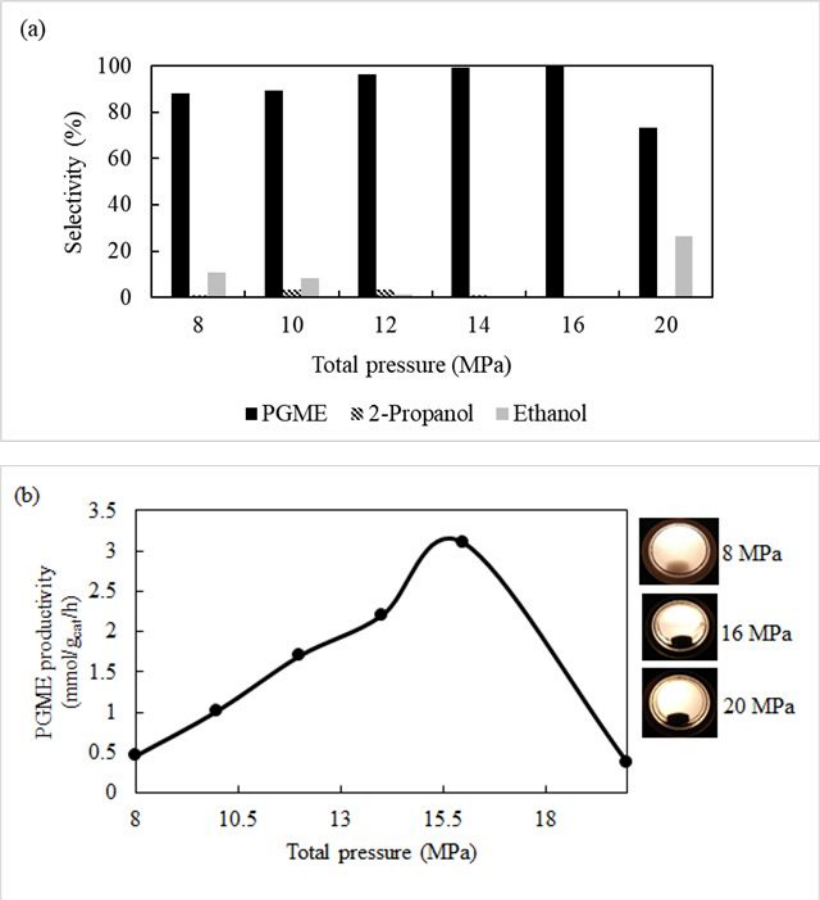
(a)
Selectivity (%)
100
80
60
40
20
0
8
10
12
14
16
20
Total pressure (MPa)
PGME
2-Propanol
Ethanol
(b)
PGME productivity (mmol/g$_{cat}$/h)
3.5
3
2.5
2
1.5
1
0.5
0
8
10.5
13
15.5
18
Total pressure (MPa)
8 MPa
16 MPa
20 MPa

Fig. 6

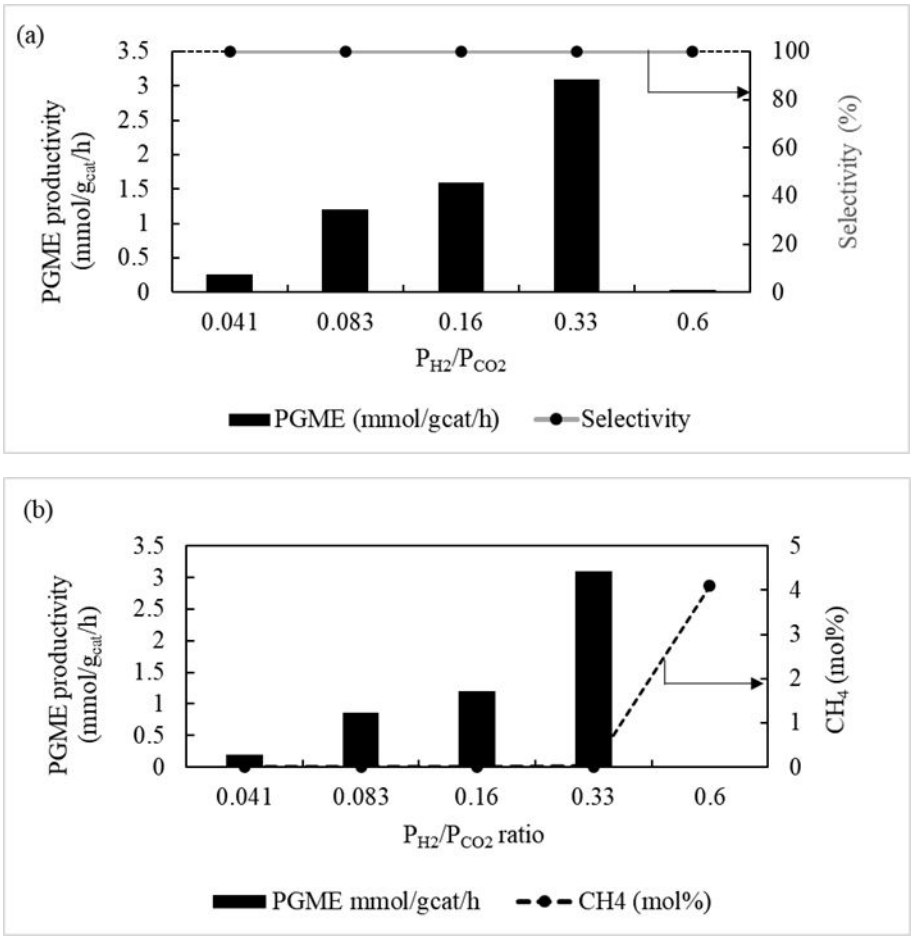
(a)
PGME productivity (mmol/g$_{cat}$/h)
Selectivity (%)
3.5
3
2.5
2
1.5
1
0.5
0
100
80
60
40
20
0
0.041
0.083
0.16
0.33
0.6
P_{H2}/P_{CO2}
PGME (mmol/gcat/h)
Selectivity
(b)
PGME productivity (mmol/g$_{cat}$/h)
CH_4 (mol%)
5
4
3
2
1
0
P_{H2}/P_{CO2} ratio
PGME mmol/gcat/h
CH4 (mol%)

Fig. 7

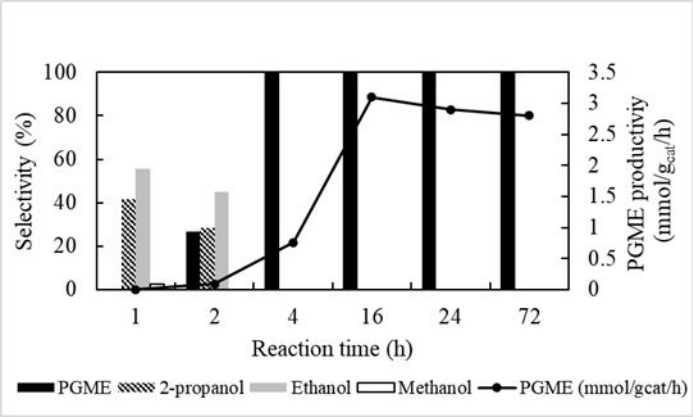
Selectivity (%)
PGME productivity (mmol/gcat/h)
Reaction time (h)
PGME
2-propanol
Ethanol
Methanol
PGME (mmol/gcat/h)

Fig. 8

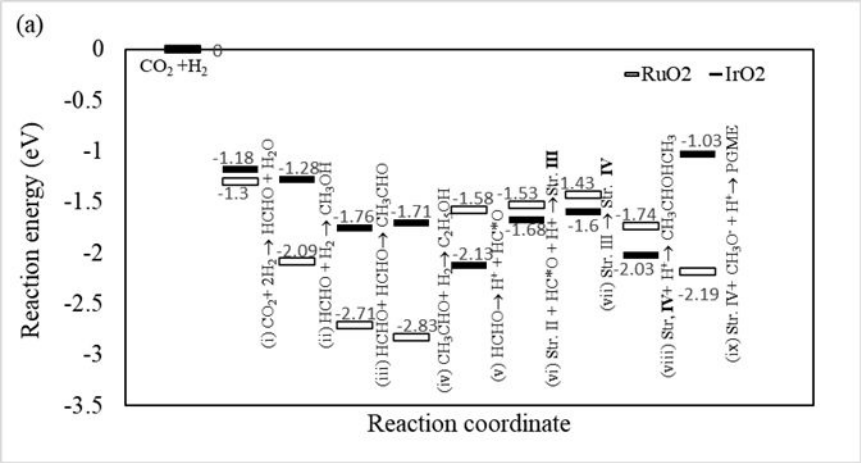
(a)
Reaction energy (eV)
Reaction coordinate
RuO2
IrO2
CO_2+H_2
0
-1.18
-1.3
-1.28
-2.09
-1.76
-2.71
-1.71
-2.83
-1.58
-2.13
-1.53
-1.68
-1.43
-1.6
-1.74
-2.03
-1.03
-2.19
(i) CO_2+ $2H_2$ → HCHO + H_2O
(ii) HCHO + H_2 → CH_3OH
(iii) HCHO+ HCHO→ CH_3CHO
(iv) CH_3CHO+ H_2→ C_2H_5OH
(v) HCHO→ H^+ + HC*O
(vi) Str. II + HC*O + H^+ → Str. III
(vii) Str. III → Str. IV
(viii) Str. IV+ H^+→ $CH_3CHOHCH_3$
(ix) Str. IV+ CH_3O^- + H^+→ PGME

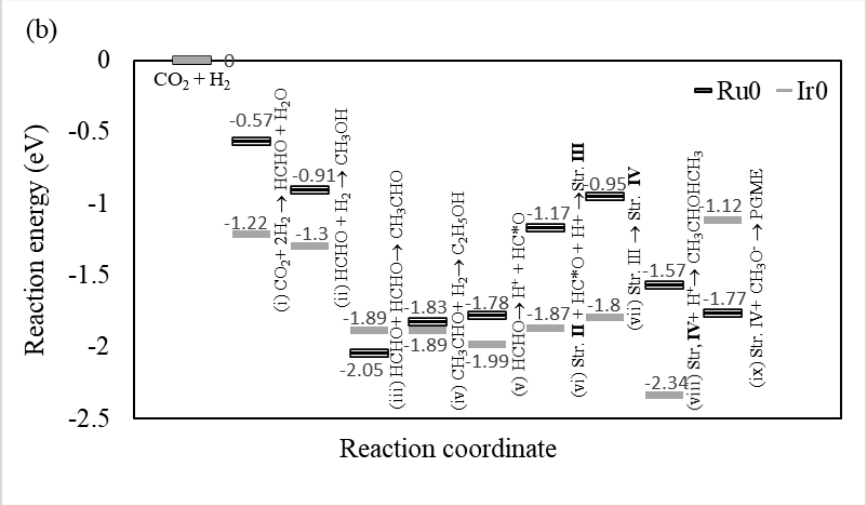
(b)
Reaction energy (eV)
Reaction coordinate
Ru0
Ir0
CO_2+H_2
0
-0.57
-1.22
-0.91
-1.3
-1.89
-2.05
-1.83
-1.89
-1.78
-1.99
-1.17
-1.87
-0.95
-1.8
-1.57
-2.34
-1.12
-1.77
(i) CO_2+ $2H_2$ → HCHO + H_2O
(ii) HCHO + H_2 → CH_3OH
(iii) HCHO+ HCHO→ CH_3CHO
(iv) CH_3CHO+ H_2→ C_2H_5OH
(v) HCHO→ H^+ + HC*O
(vi) Str. II + HC*O + H^+ → Str. III
(vii) Str. III → Str. IV
(viii) Str. IV+ H^+→ $CH_3CHOHCH_3$
(ix) Str. IV+ CH_3O^- → PGME